

1 **Serpentinization as a reactive transport process: The brucite silicification reaction**

2 Benjamin M. Tutolo^{1,*}, Andrew J. Luhmann², Nicholas J. Tosca¹, William E. Seyfried, Jr.³

3 ¹University of Oxford Department of Earth Sciences, South Parks Road, Oxford UK OX1 3AN

4 ²Department of Earth and Environmental Science, New Mexico Institute of Mining and
5 Technology, 801 Leroy Place, Socorro, NM 87801, USA

6 ³Department of Earth Sciences, University of Minnesota, 310 Pillsbury Drive SE, Minneapolis,
7 MN 55455, USA

8 *Present address: University of Calgary Department of Geoscience, 2500 University Dr. NW,
9 Calgary, AB T2N 1N4, Canada

10 **Abstract**

11 Serpentinization plays a fundamental role in the biogeochemical and tectonic evolution of the
12 Earth and perhaps many other rocky planetary bodies. Yet, geochemical models still fail to
13 produce accurate predictions of the various modes of serpentinization, which limits our ability to
14 predict a variety of related geological phenomena over many spatial and temporal scales. Here,
15 we utilize kinetic and reactive transport experiments to parameterize the brucite silicification
16 reaction and provide fundamental constraints on SiO₂ transport during serpentinization. We
17 show that, at temperatures characteristic of the sub-seafloor at the serpentinite-hosted Lost City
18 Hydrothermal Field (150°C), the assembly of Si tetrahedra onto MgOH₂ (i.e., brucite) surfaces is
19 a rate-limiting elementary reaction in the production of serpentine and/or talc from olivine.
20 Moreover, this reaction is exponentially dependent on the activity of aqueous silica ($a_{SiO_2(aq)}$),
21 such that it can be calculated according to the rate law:

22
$$Rate = 2.3 \times 10^{-4} a_{SiO_2(aq)}^{1.5} \text{ (mol/m}^2\text{/s) .}$$

23 Calculations performed with this rate law demonstrate that both brucite and Si are surprisingly
24 persistent in serpentinizing environments, leading to elevated Si concentrations in fluids that can
25 be transported over comparatively large distances without equilibrating with brucite. Moreover,
26 applying this rate law to an open-system reactive transport experiment indicates that advection,
27 preferential flow pathways, and reactive surface area armoring can diminish the net rate of Si
28 uptake resulting from this reaction even further. Because brucite silicification is a fundamentally
29 rate-limiting elementary reaction for the production of both serpentine and talc from forsterite,
30 our new constraints are applicable across the many environments where serpentinization occurs.
31 The unexpected but highly consequential behavior of this simple reaction emphasizes the need
32 for considering serpentinization and many other hydrothermal processes in a reactive transport
33 framework whereby fluid, solute, and heat transport are intimately coupled to kinetically-
34 controlled reactions.

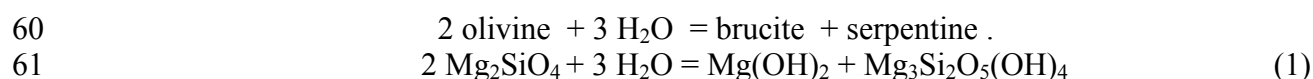
35 **1. Introduction**

36 As seawater infiltrates exhumed mantle rocks, a variety of chemical and physical
37 processes ultimately convert mafic minerals (i.e., olivine and pyroxene) to serpentine and
38 accessory phases (Evans et al., 2013; O’Hanley, 1996). For most of Earth’s history, this process,
39 known generally as “serpentinization,” has played a central role in the long-term evolution of
40 atmospheric, oceanic, and lithospheric properties. Serpentinites and serpentinite-hosted
41 hydrothermal systems host unique, microbial ecosystems (Kelley, 2005; Schrenk et al., 2013),
42 and figure prominently in chemical scenarios for the origins of life on Earth (Martin et al., 2008;
43 Sleep et al., 2011; Sojo et al., 2016) as well as in models for the early chemical evolution of the
44 atmosphere (Kump and Barley, 2007). At a broader level, serpentinizing systems strongly
45 modify the strength and rheological characteristics of the oceanic crust (Escartín et al., 2001),

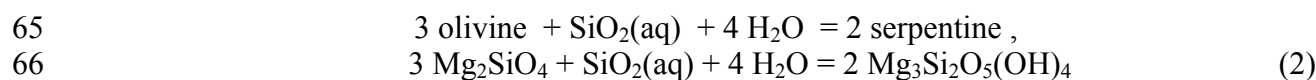
46 which, once subducted, influences both the oxidation state and water content of Earth's mantle
47 (e.g., Rüpke et al., 2004). Because the principal reactants and drivers are thought to be common
48 across a range of planetary bodies, some view serpentinization as a fundamental process
49 influencing planetary evolution more generally (e.g., Oze and Sharma, 2005; Sleep et al., 2011;
50 Waite et al., 2017).

51 Nonetheless, in spite of decades of dedicated research into serpentinization and its wide-
52 ranging implications, the various modes of serpentinization cannot yet be quantitatively
53 predicted from a process-oriented point of view. This, in turn, limits the confidence with which
54 we can extrapolate our knowledge of serpentinization over geologically relevant scales of space
55 and time.

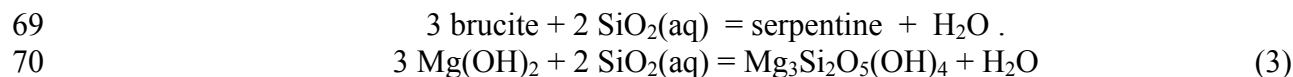
56 An important example illustrating the disparity between theoretical predictions and field
57 measurements for serpentinizing systems involves the reaction between brucite and dissolved
58 silica ($\text{SiO}_2(\text{aq})$). Considering only the magnesian end-members, the isochemical
59 serpentinization reaction may be written:



62
63 However, silica sourced from adjacent pyroxene or plagioclase often either precludes brucite
64 formation through a contemporaneous reaction:



67
68 or silicifies brucite through later-stage infiltration or a fracture reactivation event:



71

72 Through either pathway, the extreme reactivity of brucite across a broad range of SiO₂
73 concentrations dictates that either SiO₂ should be quantitatively removed from solution (if
74 brucite is the excess component) or brucite should be quantitatively converted to serpentine (if
75 SiO₂ is the excess component) (Fig. 1a). However, although petrographic studies have
76 demonstrated the operation of reactions 1-3 and their higher $a_{\text{SiO}_2(\text{aq})}$, talc-producing analogues
77 during oceanic serpentinization (e.g., Katayama et al., 2010; Klein et al., 2009), recent
78 measurements of Lost City fluids (Seyfried et al., 2015) suggest that elevated levels of SiO₂(aq)
79 can persist in serpentinizing environments, even after flowing through brucite-bearing fractures
80 and massive brucite chimney structures (Ludwig et al., 2006). This, in turn, suggests that “Lost
81 City-type” hydrothermal fluids are not always in equilibrium with their geologic surroundings,
82 and, indeed, that fluid and solute transport in concert with kinetically-controlled geochemical
83 reactions—i.e., reactive transport—govern fluid compositions observed at the seafloor.

84 Reactive transport models have long shown promise for the quantitative prediction of
85 hydrothermal processes, but this ultimate functionality has, to date, remained elusive. Amongst
86 the grand challenges in the continually evolving field of reactive transport modelling, perhaps the
87 most difficult to reconcile involves the estimation of the surface area within a particular rock that
88 will participate in a reaction, which is a function not only of the mineral’s intrinsic surface area
89 but also other factors such as flow path geometry (e.g., Helgeson et al., 1984; Noiriel et al., 2009;
90 White and Peterson, 1990). Because this fundamental parameter ultimately dictates the overall
91 pace and extent of geochemical reactions within a particular system, the accuracy of reactive
92 transport simulations hinge largely upon the accuracy of the utilized reactive surface area
93 estimate. This is particularly evident in serpentinizing systems, where most of the reactive

94 surface area within the rock is generated through feedbacks associated with flow paths generated
95 by the serpentinization reaction itself (Tutolo et al., 2016).

96 The brucite silicification reaction (reaction 3) presents a tractable yet realistic opportunity
97 to experimentally examine reactive transport processes during serpentinization and illustrate the
98 effects of reactive surface area estimates on predicted results. Here, we utilize both closed- and
99 open-system reactive transport experiments to examine the rates and evolution of this reaction at
100 150°C, a temperature characteristic of the subsurface at the Lost City Hydrothermal Field
101 (Seyfried et al., 2015), where upwelling hydrothermal fluids are interacting with serpentinized
102 oceanic crust (Früh-Green et al., 2016). We show that, although this reaction is rapid at 150°C, it
103 is orders of magnitude slower than the rates of olivine dissolution and brucite precipitation.
104 Surprisingly, strong reactive surface area feedbacks can decrease the net rate of this reaction
105 even further, in spite of continued kinetic and thermodynamic drive in its favor. This interesting
106 behavior implies that brucite and elevated $\text{SiO}_2(\text{aq})$ concentrations can be surprisingly persistent
107 in serpentinizing systems, which helps to explain the elevated $\text{SiO}_2(\text{aq})$ concentrations measured
108 at LCHF, and in turn, implies unexpected alteration phase assemblages and, potentially, limited
109 amounts of H_2 production in some serpentinizing systems

110 **2. Methods**

111 **2.1 Characterization procedures**

112 Mineral reactants for experiments were characterized by both Fourier transform infrared
113 (FTIR) spectroscopy and powder X-ray diffraction (XRD) to determine mineralogical
114 composition, and chemical composition of experimental fluids and solids were determined using
115 inductively coupled plasma-optical emission spectroscopy (ICP-OES). FTIR spectra were
116 acquired in transmission mode on optically translucent KBr disks, which were prepared by first

117 mixing ~2 mg of sample into 200 mg of dried (at 200°C) KBr powder, and then compressing the
118 mixture under vacuum to 7 tons in a hydraulic press. XRD measurements were performed at the
119 University of Oxford using a Panalytical Empyrean Series 2 outfitted with a spinning reflection-
120 transmission stage. Samples were mounted on polished silicon background substrates and
121 analyses were performed using a Co K α source at 40 kV and 40 mA. 5-point Brunauer-Emmett-
122 Teller (BET) specific surface area was measured with N₂ gas on the brucite powder (dried at
123 60°C) used in the closed-system experiments at the University of Oxford Begbroke Science
124 Park. The measured specific surface area, 5.41 ± 0.06 m²/g, was used to calculate the silica
125 uptake rate in the closed-system experiments.

126 Mg, Ca, Na, and SiO₂ concentrations in selected fluid samples and the solid brucite ore
127 used in the open-system reactive transport experiment were analyzed by ICP-OES at the Scottish
128 Universities Environmental Research Centre in Glasgow, UK (for the closed-system
129 experiments) and in the University of Minnesota Department of Earth Sciences (for the reactive
130 transport experiment). In the closed-system experiments, Ca concentrations were below the
131 detection limit and variations in Na concentration were smaller than analytical errors and hence
132 neither element is reported. In several samples from the flow-through experiment, SiO₂ was
133 measured spectrophotometrically using the molybdate blue method with metol as the reducing
134 agent (Mullin and Riley, 1955) in order to supplement data provided by ICP-OES. Solution pH
135 was measured using a Thermo Scientific™ Orion™ 8103BN ROSS™ Combination semi-micro
136 (Oxford) or micro (Minnesota) pH electrode, calibrated using NIST-traceable 7 and 10 pH
137 buffers. X-ray computed tomography (XRCT) imaging was performed on the core assembly
138 described below in the University of Minnesota XRCT laboratory in order to infer extents of
139 physical and chemical evolution that occurred over the course of the flow-through experiment.

140 The core assembly was imaged in a dry state prior to the experiment, and subsequently imaged in
141 a water-saturated state directly after the experiment and again after it had been flushed with
142 deionized water and dried at 60°C. The dry core images showed significantly better grayscale
143 contrast than the water-saturated images without any noticeable difference in other volume
144 features and are thus used exclusively in experimental interpretations below. In addition, pre-
145 and post-experiment subsamples of the fracture fill material were analyzed using a Scanning
146 Electron Microscope (SEM) coupled to an Energy Dispersive Spectrometer in the
147 Characterization Facility at the University of Minnesota.

148 **2.2 Experimental Methods**

149 The goal of this study is to provide insight into the reactive transport process of
150 serpentinization using experimental observations of the elementary brucite silicification reaction.
151 Because no data exist within the literature to calculate the rate of this reaction in even ideal
152 conditions, we first present a series of well mixed, closed-system experiments to quantify its rate.
153 The measured evolution of fluid chemistry as a function of time during these closed-system
154 experiments permits the derivation of a rate law for calculating the rate of silica depletion during
155 brucite silicification as a function of brucite surface area and the activity of aqueous silica.
156 Subsequently, we present an open-system reactive transport experiment that inherently
157 incorporates reactive transport processes, such as surface area armoring and preferential flow
158 pathways. The parameterization derived from the closed-system experiments enables the
159 quantitative interpretation of surface area evolution during the open-system reactive transport
160 experiment. Together, these experimental results provide direct insight into serpentinization in
161 natural systems.

162 **2.2.1 Closed-system experiments**

163 Reactant fluid in all experiments was prepared to match seawater chloride concentration
164 (0.547 mol Cl/kg solution) by addition of reagent grade NaCl. Consistent with the absence of
165 measurable Mg in LCHF vent fluids (Seyfried et al., 2015), the experimental solutions contained
166 no Mg and were hence undersaturated with respect to the reactant brucite. Other species typical
167 to seawater and the LCHF vent fluids, such as Ca, K and SO₄, were also left out of reactant
168 solutions because they are not expected to impact the progress of the focus brucite silicification
169 reaction.

170 Closed-system reactor experiments were performed at the University of Oxford in a 100 mL
171 pressure vessel manufactured by the Parr Instrument Company (Model 4793). All internal
172 wetted parts are constructed of inert Ti, which were heated in air at 350°C for ~4 hours prior to
173 the experiments in order to produce a thin, oxidized surface coating. A flat PTFE gasket creates
174 a seal between the upper and lower portions of the reaction vessel, which was heated by an
175 external band heater coupled to a K-type thermocouple inserted into a Ti well in direct contact
176 with the reactant fluid. Internal pressure is equilibrium steam saturation pressure, ~4.8 bar.
177 High-purity (95%) brucite (102 mg and 105 mg for Expts. 3 and 4, respectively) and a PTFE-
178 coated stir bar were loaded into the vessel prior to sealing. Once sealed, the vessel was secured
179 in an upright position on a magnetically controlled stirrer, the experimental fluid (75.75 g and
180 75.43 g in Expts. 3 and 4, respectively) was injected through a port in the top of the vessel, and
181 the temperature controller was set to 150°C. Total time between fluid loading and reaching
182 150°C was ~20-25 minutes. Throughout the experiments, fluid samples (~1 mL) were obtained
183 through a Ti dip tube fitted with a 10 µm Ti filter positioned within the reactant fluid in order to
184 observe the real-time evolution of fluid chemistry within the vessel. Each fluid sample was
185 preceded by a ~1 mL rinse sample in order to clear stagnant fluid from within the dip tube prior

186 to sample acquisition, causing the total mass of reactant fluid to decrease by ~2 mL after each
187 sample and the fluid/solid ratio to decrease accordingly. Rate calculations take these masses into
188 account. pH was measured on a ~0.5 mL aliquot immediately upon sampling, and the remainder
189 of the sampled fluid was acidified and diluted to preserve for later analyses.

190 In two initial experiments (Expts. 1 and 2), the initial $\text{pH}_{21^\circ\text{C}}$ of the reactant solution was set
191 to ~8 in order to approximate the pH of seawater, and SiO_2 concentration of the initial reactant
192 fluid was set to amorphous silica saturation (~1.8 mmol/kg solution (Gunnarsson and Arnórsson,
193 2000)) using Na metasilicate nonahydrate ($\text{Na}_2\text{SiO}_3 \cdot 9\text{H}_2\text{O}$). However, approximately half of
194 this SiO_2 was removed prior to reaching 150°C , preventing acquisition of meaningful rate data.
195 These experiments will not be discussed further. The presented experiments (Expts. 3 and 4)
196 were performed with an initial $\text{pH}_{21^\circ\text{C}} \approx 9.8$, which, because it is near the pK for silicic acid at
197 room temperature (~9.86), permitted a much higher initial $\text{SiO}_2(\text{aq})$ concentration without
198 precipitating amorphous silica. Although quartz was ~2x supersaturated in the initial samples
199 from both closed-system experiments, the rate of quartz precipitation this close to equilibrium is
200 slow (Rimstidt and Barnes, 1980) and we therefore do not expect that precipitation of this
201 mineral could have affected our results. In order to capture the rapid rates of reaction at high
202 $\text{SiO}_2(\text{aq})$ concentrations, an aggressive sampling protocol was planned for Expt. 3, such that a
203 total of 9 samples were taken within the first 3 hours. Expt. 4 was sampled less frequently and
204 hence was able to continue for longer prior to termination while maintaining similar volumes of
205 experimental fluid.

206 **2.2.2 Reactive transport experiment**

207 A single-pass, hydrothermal flow-through apparatus (Fig. 2a) located in the University of
208 Minnesota Department of Earth Sciences, which has been described in several previous studies

209 (Luhmann et al., 2017, 2014; Tutolo et al., 2015), was utilized to examine the effect of reactive
210 transport processes on the brucite silicification reaction (Fig. 1b). In brief, the apparatus makes
211 use of a set of 4 Teledyne Isco syringe pumps to facilitate fluid injection and pressurization. A
212 constant outlet pressure (150 bars in this study) is controlled by a model 500D pump, constant
213 confining pressure (200 bars in this study) is maintained by a model 260D pump, and an
214 additional set of 2 model 260D pumps are used to inject the experimental solution at a constant
215 rate (0.05 mL/min in this study) into the core assembly, which is contained within a stainless
216 steel pressure vessel. In the present study, the pressure vessel was maintained at 150°C
217 throughout the duration of the experiment by a set of 4 thermocouple-linked Watlow band
218 heaters. While flowing through the heated pressure vessel and reacting with the brucite, the
219 experimental solution only contacted corrosion-resistant pieces made from titanium, Teflon, and
220 PEEK. Permeability was continuously measured during the experiment, and fluid samples were
221 collected after passing through the core. Furthermore, a set of two inert Ti separators with
222 internal, o-ring sealed Ti pistons were utilized on the upstream and downstream side of the
223 pressure vessel in order to prevent the corrosive reactant fluid from coming into contact with the
224 stainless steel interior of the syringe pumps. During typical experiments run with this apparatus
225 (e.g., Luhmann et al., 2014), deionized water is flowed through the core at room temperature
226 prior to the experiment in order to establish baseline permeability. However, in this study, due to
227 the high reactivity of brucite in deionized water at even room temperature, this could not be done
228 without potentially dissolving significant brucite. Thus, the core was pressurized immediately
229 prior to experiment initialization.

230 To facilitate digitization and approximate the fractures characteristic of serpentization
231 environments, we designed a special Teflon PTFE core assembly with a planar, 1.5 mm x 24.9

232 mm x 11.34 mm section of the cylindrical “core” filled with ground brucite ore, held in place
233 with Ti frit endcaps (Fig. 2b). This natural brucite, from Brucite Mine, Nevada, was analyzed by
234 ICP-OES to contain 62.2% MgO, 2.8% CaO, 2.0% SiO₂, and 0.6% FeO. It consisted of 90-95%
235 brucite, minor Mg-bearing carbonates, and trace lizardite and was previously used for
236 carbonation experiments by Harrison et al. (2013). The material was first ground and then wet-
237 sieved to select particles in the 75 μm-150 μm size range, which were aggregates of many much
238 smaller brucite particles (Fig. 2c), as evidenced by their complete disaggregation during an initial
239 attempt to sonicate them to remove surface particles. A total of 781 mg (dry mass) of brucite was
240 loaded into the core assembly and loaded into a cylindrical Teflon sheath. Assuming a brucite
241 density of 2.368 g/cm³ (Robie and Hemingway, 1995), the total porosity of the planar fracture
242 was 0.22, and this value is assumed to be constant in the relevant calculations below. Harrison
243 et al. (2013) report a specific surface area of 6.6 m²/g for this material, and we utilize this value
244 for the relevant calculations below. The reactant solution in this experiment was a 547 mmol
245 NaCl/kg seawater analogue solution, to which 1.7 mmol SiO₂/kg had been added in the form of
246 silica gel. To facilitate silica dissolution into the solution, we initially raised the pH of the
247 solution above 10 and heated it in a sealed polyethylene bottle to 60°C for several days. The
248 pH_{21°C} solution was then lowered to 8 by HCl addition in order to simulate the pH of seawater.
249 In total, 500 mL (i.e., the approximate total volume of the two injection pumps) of fluid were
250 injected into the core over the course of the experiment, yielding a cumulative water-to-rock
251 mass ratio of ~640. The Darcy velocity in this experiment, ~1550 m/yr, is reasonable, given the
252 (limited) constraints on fluid residence times at T > 150°C in mid-ocean ridge hydrothermal
253 systems (1-3 years (Kadko and Butterfield, 1998)) and an assumed upflow path at LCHF of less
254 than several kilometers (e.g., Seyfried et al., 2015).

255 2.3 Theoretical treatment of rate data

256 In treating the closed-system experiments, we assumed that the brucite silicification
257 reaction behaves according to the following form of the rate law:

$$258 \text{Rate} = k A a_{\text{SiO}_2(\text{aq})}^n \quad (4)$$

259 where k is the rate constant for the reaction, A is the surface area of the reactant brucite, and n is
260 the reaction order with respect to the activity of aqueous silica ($a_{\text{SiO}_2(\text{aq})}$). Equation 4 has the
261 same general form as that derived for the geochemically analogous kaolinite illitization reaction
262 by Chermak and Rimstidt (1990). Following the methodology described by Chermak and
263 Rimstidt (1990), we evaluated the reaction order with respect to $a_{\text{SiO}_2(\text{aq})}$ by calculating the Si
264 removal rate in the closed system experiments according to:

$$265 \text{rate} = \frac{\Delta C_{\text{Si}} m_{\text{soln}}}{\Delta t A} \quad (\text{mol}/\text{m}^2/\text{s}) \quad (5)$$

266 where ΔC_{Si} is the measured change in Si concentration, m_{soln} is the mass of solution in the
267 reactor, taking into account mass changes due to sampling, Δt is the time between samples, and A
268 is again the surface area of brucite in the reactor, calculated as the product of the measured BET
269 specific surface area and the mass of brucite in the reactor. Attempts to approximate reductions
270 in brucite surface area in the reactor according to stoichiometric Mg-silicate-forming reactions
271 had no effect on the calculated reaction order or rate constant within the uncertainty of the
272 calculation and hence were ignored. This is consistent with the limited amount of reaction
273 permitted stoichiometrically (Reaction 3 and its talc-producing analogue, which requires 1.33
274 moles of $\text{SiO}_2(\text{aq})$ per mole of brucite) between the 1.8 total millimoles of brucite in the reactor
275 and the ~350 total micromoles of Si removed from solution.

276 Uncertainties on calculated rates were calculated using standard procedures (Rimstidt, 2014),
277 taking into account the standard deviation of measured Si concentrations and uncertainty on BET
278 surface area. Regression of rates as a function of $a_{SiO_2(aq)}$ was performed according to York et
279 al. (2004), taking into account uncertainties on both calculated $a_{SiO_2(aq)}$ (assumed equivalent to
280 the standard deviation of the measured Si concentrations) as well as the uncertainties on the rates
281 calculated using Eqn. 5. We optimized the value of k using an iterative, nonlinear least squares
282 data fitting procedure which minimized the difference between the measured number of moles of
283 SiO₂ removed from solution (Table 1) and those calculated using Eqn. 4. In order to remove bias
284 introduced by the variable period between individual samples, a spline function was fit to the
285 measured values as a function of time, and the data were resampled at 10, 100, and 1000 evenly
286 spaced intervals. A significant change in the value of the rate constant was observed between 10
287 and 100 samples, but not between 100 and 1000 samples, thus, the reported rate constant is the
288 value obtained after fitting to 1000 evenly spaced subsamples.

289 **2.4 Numerical methods**

290 The Geochemist's Workbench version 10.0.10 (Bethke and Yeakel, 2015) and
291 PFLOTRAN (Lichtner et al., 2017) were utilized for aqueous speciation and reactive transport
292 calculations, respectively. Because this study focuses on the role of silica in serpentinization
293 reactions, it is important to ensure that the data that we are using to produce thermodynamic
294 calculations of fluid-mineral equilibria agree with available data for the aqueous speciation of
295 silica over the range of temperatures and pressures applicable to serpentinization reactions. As
296 discussed in detail in Tutolo and Tosca (in review), a geochemical thermodynamic database
297 taking explicit account of recent revisions to the speciation of aqueous silica was created using
298 the DBCreate software package (Kong et al., 2013). Briefly, this database was created using

299 updated $\text{SiO}_2(\text{aq})$ thermodynamic properties presented by Sverjensky et al. (2014), which are
300 consistent with the updated low-temperature quartz solubility measurements of Rimstidt (1997).
301 The $\text{NaHSiO}_3(\text{aq})$ complex was removed from the database due to revised experimental
302 measurements that have drawn its stability in seawater into question (Busey and Mesmer, 1977;
303 Felmy et al., 2001; Zarubin and Nemkina, 1990). This complex has a major effect on the
304 aqueous speciation of silica and the overall solubility of silicate minerals at $\text{pH} > \text{pK}$ for silicic
305 acid (see Tutolo and Tosca, in review) and it is thus particularly important to avoid including it
306 in aqueous speciation calculations of water-rock interaction in ultramafic-hosted systems.

307 **3. Results and discussion**

308 The conversion of brucite to serpentine (reaction 3) can be conceptualized through a
309 simple, epitaxial reaction (Carrado et al., 2000): Si tetrahedra from solution bind to the surface of
310 octahedrally coordinated Mg (in the form of brucite), forming serpentine (at higher $a_{\text{SiO}_2(\text{aq})}$, the
311 resultant mineral is talc (Fig. 1), but the mechanism is identical). This process is exemplified by
312 the results of our closed-system experiments. Specifically, the observed concentrations
313 Nonetheless, in the open-system reactive transport experiment, which was designed to more
314 closely approximate processes characteristic of natural serpentinizing environments, the fluids
315 and reactants are clearly not well-mixed, and only a relatively small proportion of the total
316 brucite surface area is accessible to the flowing fluid. As discussed below, the closed-system
317 experiments provide constraints on the surface-controlled process of brucite silicification under
318 well-mixed conditions, and the laboratory and numerical reactive transport experiments allow us
319 to observe how reactive transport processes can affect the rate and extent of this reaction.

320 **3.1 Closed System Experiments**

321 In spite of the experimental challenges associated with the brucite silicification reaction,
 322 our closed-system experiments provide mutually consistent rate measurements, which, in turn,
 323 permit kinetic parameterization. Solution analyses indicate Mg concentrations near detection
 324 limits in all samples, which is expected, given that equilibrium brucite solubility in our
 325 experimental solutions at $\text{pH}_{150^\circ\text{C}} = 8.2$ is $\sim 10 \mu\text{mol/kg}$. Thus, within the uncertainty on our
 326 calculated $\text{pH}_{150^\circ\text{C}}$ (on the order of ± 0.1 pH unit), the solutions were very close to
 327 thermodynamic equilibrium with respect to brucite. Although the $\text{pH}_{150^\circ\text{C}}$ of all samples from
 328 both experiments (Table 1) is above the neutral $\text{pH}_{150^\circ\text{C}} (\approx 5.8)$, they are all below the $\text{p}K_{150^\circ\text{C}}$ for
 329 silicic acid (8.75) such that $\text{SiO}_2(\text{aq})$ accounts for the majority ($\sim 70\%$) of the total aqueous silica
 330 in the analyzed solutions, with the remainder existing as HSiO_3^- . The initial samples in both
 331 experiments are characterized by a notably more rapid rate of reaction than the subsequent
 332 samples, consistent with an exponential dependence of the reaction rate upon $a_{\text{SiO}_2(\text{aq})}$ according
 333 to Eqn. 5. Fitting a line to a plot of the rates calculated according to Equation 4 as a function of
 334 the $a_{\text{SiO}_2(\text{aq})}$ in solution (Fig. 3a) yields the equation:

$$335 \quad \log(r) = 1.55(0.08) \log a_{\text{SiO}_2(\text{aq})} - 3.39(0.28), \quad (6)$$

336 where the values in parentheses are the calculated standard error. This result suggests a reaction
 337 order (n) of 1.5 with respect to with respect to $a_{\text{SiO}_2(\text{aq})}$, and subsequent fitting of Eqn. 4 to the
 338 measured SiO_2 concentrations yields the rate law:

$$339 \quad \text{Rate} = 2.3 \times 10^{-4} a_{\text{SiO}_2(\text{aq})}^{1.5} \text{ (mol/m}^2\text{/s)}, \quad (7)$$

340 which is applicable at 150°C for values of $a_{\text{SiO}_2(\text{aq})}$ at least down to $\sim 10 \mu\text{molal}$ at seawater ionic
 341 strength. Assuming 1 m^2 of brucite interacting with 1 kg of solution, these data indicate that it
 342 would take 5.25 days to reduce the $\text{SiO}_2(\text{aq})$ concentration from 1.7 mmol/kg to $170 \mu\text{mol/kg}$,
 343 another 16.6 days to reach $17 \mu\text{mol/kg}$ and another 52.4 days to remove the 15.3 micromoles of

344 Si required to achieve a concentration of 1.7 $\mu\text{mol/kg}$. Regardless of the applicability of these
345 specific water-to-rock ratios, the calculations indicate that significant disequilibrium can be
346 maintained during SiO_2 transport through serpentinizing rocks. For example, at $a_{\text{SiO}_2(\text{aq})} \approx 73$
347 $\times 10^{-6}$ (i.e., the end-member concentration measured in 116°C vent fluids at the Lost City
348 Hydrothermal Field (Seyfried et al., 2015)), Eqn. 7 yields a reaction rate of $\sim 1 \times 10^{-10}$ $\text{mol/m}^2/\text{s}$,
349 which is several orders of magnitude slower than the 150°C dissolution rates of brucite, 8.6×10^{-7}
350 $\text{mol/m}^2/\text{s}$ (Palandri and Kharaka, 2004) and forsterite, $\sim 1 \times 10^{-6}$ $\text{mol/m}^2/\text{s}$ (Rimstidt et al., 2012).
351 Assuming that brucite growth rates are within 1-2 orders of magnitude of its dissolution rates (as
352 shown experimentally by Pokrovsky and Schott (2004) at 25°C), this comparison confirms that
353 the assembly of silica tetrahedral sheets onto Mg octahedral sheets (i.e., brucite) is the rate-
354 limiting step during forsterite serpentinization. This assertion is in agreement with the
355 experimental observations of Lin and Clemency (1981) and Saldi et al. (2007), who suggested
356 that the rate-limiting step of the reverse reaction (i.e., antigorite and talc *dissolution*) is the
357 destruction of tetrahedral Si rather than octahedral Mg sheets.

358 All fluid samples from both closed-system experiments were within the chrysotile
359 stability field in $a_{\text{Mg}^{++}}/a_{\text{H}^+}^2 - a_{\text{SiO}_2(\text{aq})}$ space, but the majority of the samples were above the
360 $a_{\text{SiO}_2(\text{aq})}$ for talc-chrysotile equilibrium, i.e., 200×10^{-6} (Fig. 1a). Solids recovered from Expt. 3
361 showed no crystallographic evidence of silicification, consistent with its relatively short duration
362 and extent of reaction. XRD data from Expt. 4, on the other hand, exhibit a low-angle peak at
363 ~ 10.2 Å, consistent with the formation of kerolite, a hydrated, structurally-related form of talc.

364 **3.2 Reactive transport experiment**

365 In total, 0.87 millimoles of dissolved SiO_2 were injected into the synthetic, brucite-filled
366 fracture during the reactive transport experiment. Models assuming equilibrium between well-

367 mixed reactants and products predict that the 13.4 millimoles of brucite within the synthetic
368 fracture would deplete Si well below detection levels during flow through the core (see below).
369 Nonetheless, solution chemical analyses consistently indicate SiO₂ concentrations well above
370 those required for brucite stability exiting the experimental reactor during the first ~110 hours of
371 the experiment, and a subsequent, rapid transition to even lower net reactivity (Table 2, Fig. 4a).
372 At the conclusion of the experiment, ~0.62 of the total injected 0.87 millimoles of SiO₂ had been
373 deposited within the core. Assuming serpentine growth (see mineralogical constraints below),
374 this amount of silica uptake accounts for the reaction of ~0.41 millimoles, or ~3%, of the brucite
375 contained within the synthetic fracture.

376 Mg concentrations in outlet fluids varied from an early-time maximum of 2.3 mmol/kg,
377 down to a minimum of ~44 μmol/kg. These solutions tend to be ~1-2 orders of magnitude
378 undersaturated with respect to brucite and near equilibrium or supersaturated with respect to
379 chrysotile (Table 2). These results, particularly the generally low Mg concentrations and the
380 relatively low supersaturations of chrysotile in the bulk fluid, are consistent with the reaction
381 mechanism discussed above, wherein serpentine is crystallizing by silica condensation upon to
382 brucite surfaces, rather than through heterogeneous crystallization from the bulk fluid phase.

383 In spite of the surface area effects discussed below, the main reason that SiO₂
384 concentrations above brucite-serpentine equilibrium are exiting the brucite-filled fracture during
385 the first 110 hours of the experiment is the exponential dependence of the silicification reaction
386 on $a_{SiO_2(aq)}$, as discussed in the previous section. Fig. 4b illustrates the expected surface area-
387 normalized silica uptake rates for the solution samples plotted in Fig. 4a. As a result of this
388 exponential rate dependency, the outlet solutions sampled during the first ~110 hours of the
389 experiment have an expected reaction rate ~2 orders of magnitude lower than that calculated for

390 the injected solution, showing that elevated concentrations of Si can persist even as the solution
391 flows through a packed bed of high-surface-area brucite. After 110 hours of experiment time,
392 however, the outlet SiO₂ concentrations indicate that there is simply much less brucite surface
393 area reacting with the fluid. Even though the bulk of fluid flow during this experiment was
394 apparently confined to a relatively limited portion of the fracture, this result is quite surprising
395 because: 1) XRD and FTIR both indicate that even this more reactive portion of the synthetic
396 fracture was still composed almost entirely of brucite after the experiment, and 2) no apparent,
397 abrupt change in the permeability of the synthetic fracture occurred at this time, which would
398 have represented either significant porosity decreases due to serpentine growth or a change in the
399 dominant fluid flow path within the core (Fig. 5). The decline in permeability measured at the
400 beginning of the experiment, significantly prior to the change in reaction regimes, is consistent
401 with pressurization and compaction of the brucite fracture fill, since the pressurization of the
402 core assembly occurred simultaneously with experiment initialization. Because the fluid
403 injection rate was constant throughout the experiment, this permeability did not directly impact
404 fluid residence time within the reactor.

405 We have labeled the transition from the first reaction regime to the second as
406 “precipitation breakthrough”, due to the analogy to “dissolution breakthrough” processes which
407 occur whenever high permeability, low reactivity preferential flow paths are generated in, for
408 example, carbonate aquifers (e.g., Dreybrodt, 1990). Regardless of the mechanism, the fact that
409 such high concentrations of SiO₂ are exiting the reaction vessel indicates that very little brucite
410 surface area was available for reaction during this stage of the experiment, in spite of the fact that
411 abundant brucite remained both in the “reacted” and “unreacted” regions of the core. Although
412 the small amount of serpentine formed during the experiment precludes identification by XRD,

413 the location and topology of the set of peaks at 988 and 1087 cm^{-1} in the post-experiment FTIR
414 spectrum demonstrate serpentine precipitation (Fig. 6c). These principal Si-O absorptions are
415 distinct from all other 2:1 phyllosilicates or modulated versions thereof (i.e., talc, kerolite,
416 sepiolite, etc.; (Farmer, 1974; Russell and Fraser, 1994)) and are instead indicative of poorly
417 crystalline serpentine, akin to the poorly crystalline antigorite identified by Gunnarsson et al.,
418 (2005, 2002) and the proto-serpentine discussed by Andreani et al. (2007) and Plümper et al.
419 (2012).

420 **3.3 Reactive transport simulations of brucite silicification**

421 By incorporating the rate law determined above into reactive transport simulations of our
422 flow-through experiment, we can hone in on specific reactive transport phenomena occurring
423 during the experiment. This allows us to fully understand the implications of the quantified
424 brucite silicification reaction for reactive transport in natural serpentinites. To do this, we ran a
425 series of 200 PFLOTRAN simulations that examine the effects of preferential flow paths and
426 reactive surface area armoring on silica uptake. These simulations illustrate that no more than
427 about 15% of the brucite surface area in the synthetic fracture participated in the reaction at any
428 given time (Fig. 7a). Indeed, during the post-precipitation breakthrough reaction regime, very
429 little (i.e., less than $\approx 1\%$) of the brucite contained within the core assembly was participating in
430 the reaction, most likely because the easily accessible surface area within this portion of the core
431 had been virtually completely silicified by this time. If, on the other hand, all of the brucite in
432 the synthetic fracture had been participating in the reaction, outlet concentrations would have
433 been on the order of 1 μmolal , or about double the concentration representative of brucite-
434 serpentine equilibrium, and about 50 times lower than the lowest measured concentration. In
435 spite of the fact that only about 1/3 of the fracture showed evidence of silicification in post-

436 experiment imagery (Fig. 6), these simulations show that even within this portion of the core,
437 only a fraction of the brucite was actually participating in the reaction. This latter observation is
438 consistent with the limited (~3%) extent of brucite conversion to serpentine calculated above.

439 The results of these simulations also clearly illustrate the progress of brucite silicification
440 during fluid transport through the core (Fig. 7b). It is particularly interesting to observe the ways
441 in which the coupling between advective Si fluxes, $a_{SiO_2(aq)}$, and brucite reactive surface area
442 availability interact to produce unique equilibration length scales in serpentinizing rocks. For
443 example, these simulations show that in high-flux environments, such as faults, where reactive
444 surface area has been depleted by long-duration fluid fluxes, Si can be transported over great
445 distances and, thus, seafloor samples of these fluids would be quite representative of the
446 subseafloor reaction zone. At the other end of the spectrum, at the scales of individual olivine
447 crystals (i.e., several hundred micrometers), these simulations show that high Si concentrations
448 generated by orthopyroxene-fluid interaction, such as those producing the pattern of
449 serpentinization shown in Fig. 1, can be laterally persistent if rates of advection/diffusion are
450 sufficiently high, or if the existing brucite surface area has been largely armored during prior
451 stages of serpentinization. These two scales of observation can both be tackled with
452 appropriately scaled reactive transport models, and demonstrate the usefulness of treating
453 serpentinization in a reactive transport sense.

454 **5. Geological Implications**

455 The efficiency and pathway of serpentinization can be dictated by a wide array of
456 processes, yet our study offers unique perspectives on the geological mechanisms that underlie
457 the reactions themselves. From an entirely kinetic point of view, our rate data show that the slow
458 rate of brucite silicification relative to both forsterite dissolution and $MgOH_2$

459 dissolution/precipitation allows elevated (i.e., above brucite-serpentine equilibrium)
460 concentrations of Si to persist in moderate-temperature serpentinization environments. That the
461 rate of brucite silicification slows as an exponential function of $a_{SiO_2(aq)}$ indicates that Si can be
462 transported over comparatively large length scales, particularly when considering the reactive
463 transport processes we have discussed.

464 Both our laboratory and numerical reactive transport experiments illustrate that
465 traditional geochemical models of serpentinization cannot produce accurate, process-oriented
466 predictions of serpentinizing systems. For example, the presence of brucite in serpentinized
467 rocks has been used to infer excessively low concentrations of SiO_2 concentrations in reacting
468 fluids (e.g., Beard and Hopkinson, 2000). In addition, at face value, simplified rate formulations
469 (e.g., Martin and Fyfe (1970)) and the activity diagram plotted in Fig. 1 would appear to suggest
470 that serpentinization should proceed rapidly and irreversibly in all seafloor hydrothermal
471 systems, with brucite fully reacting out in the presence of even negligible aqueous silica.
472 However, we have shown that the exponential dependence of the rate of this reaction on
473 $a_{SiO_2(aq)}$, as well as reactive surface area armoring, permit SiO_2 concentrations to remain
474 metastably elevated. As a consequence, these dynamic factors allow brucite to persist in such
475 systems, particularly when the brucite surfaces are separated from primary flow paths by
476 serpentine. From the fluid perspective, our results also help to explain recent reports of elevated
477 Si fluids emitting from orifices in the massive brucite chimneys at the Lost City Hydrothermal
478 Field (Seyfried et al., 2015). Because elevated Si fluxes in serpentinizing environments are
479 thought to govern the partitioning of Fe into alteration phases and, consequently, the amount of
480 H_2 generated from Fe oxidation (Bach et al., 2006; Frost and Beard, 2007; Syverson et al., 2017),
481 our new kinetic and reactive transport constraints suggest that elevated Si and its consequent

482 effects on H₂ production and biological habitability can be surprisingly prevalent in
483 serpentinizing environments.

484 Brucite silicification is a fundamentally rate-limiting elementary reaction for the
485 production of both serpentine and talc from forsterite. Thus, our new constraints are applicable
486 across the many environments where serpentinization occurs. The surprising kinetic behavior of
487 this simple reaction, in turn, emphasizes the need for considering serpentinization and many
488 other hydrothermal processes as reactive transport processes in which fluid, solute, and heat
489 transport are intimately coupled to kinetically-controlled serpentinization reactions. Persistent
490 challenges in the application of reactive transport models to geologic systems, particularly the
491 estimation of reactive surface area within geologic media, will thus need to be the subject of
492 continued, focused experimental and computational investigations.

493 **Acknowledgements**

494 This research used samples and/or data provided by the International Ocean Discovery Program
495 (IODP). Portions of this research were supported by the United States National Science
496 Foundation under grant number 1426695. We thank Glenn Hammond for help with the
497 PFLOTTRAN simulations, Nicholas Seaton for assistance with SEM analysis, Brian Bagley for
498 assistance with XRCT imaging and processing, and Anna Harrison for providing the brucite used
499 in the reactive transport experiment. The Characterization Facility at the University of
500 Minnesota, where the SEM imaging was performed, receives partial support from NSF through
501 the MRSEC program. The authors wish to thank two anonymous reviewers and Associate Editor
502 Mike Bickle, whose critical evaluation of this manuscript helped to improve its clarity.

503

504 **References**

505 Bach, W., Paulick, H., Garrido, C.J., Ildefonse, B., Meurer, W.P., Humphris, S.E., 2006.
506 Unraveling the sequence of serpentinization reactions: Petrography, mineral chemistry, and
507 petrophysics of serpentinites from MAR 15°N (ODP Leg 209, Site 1274). *Geophys. Res.*
508 *Lett.* 33, 4–7. doi:10.1029/2006GL025681

509 Beard, J.S., Hopkinson, L., 2000. A fossil, serpentinization-related hydrothermal vent, Ocean
510 Drilling Program Leg 173, Site 1068 (Iberia Abyssal Plain): Some aspects of mineral and
511 fluid chemistry. *J. Geophys. Res.* 105, 16,527–16,539. doi:10.1029/2000JB900073

512 Bethke, C.M., Yeakel, S., 2015. The Geochemist's Workbench® Release 10.0 - Reference
513 Manual.

514 Busey, R.H., Mesmer, R.E., 1977. Ionization equilibriums of silicic acid and polysilicate
515 formation in aqueous sodium chloride solutions to 300.degree. {C}. *Inorg. Chem.* 16, 2444–
516 2450. doi:10.1021/ic50176a004

517 Carrado, K.A., Xu, L., Gregory, D.M., Song, K., Seifert, S., Botto, R.E., 2000. Crystallization of
518 a layered silicate clay as monitored by small-angle X-ray scattering and NMR. *Chem.*
519 *Mater.* 12, 3052–3059. doi:10.1021/cm000366a

520 Chermak, J.A., Rimstidt, J.D., 1990. The hydrothermal transformation rate of kaolinite to
521 muscovite/illite. *Geochim. Cosmochim. Acta* 54, 2979–2990. doi:10.1016/0016-
522 7037(90)90115-2

523 Dreybrodt, W., 1990. The Role of Dissolution Kinetics in the Development of Karst Aquifers in
524 Limestone: A Model Simulation of Karst Evolution. *J. Geol.* 98, 639–655.
525 doi:10.1086/629431

526 Escartín, J., Hirth, G., Evans, B., 2001. Strength of slightly serpentinized peridotites:

527 Implications for the tectonics of oceanic lithosphere. *Geology* 29, 1023–1026.
528 doi:10.1130/0091-7613(2001)029<1023:SOSSPI>2.0.CO

529 Evans, B.W., Hattori, K., Baronnet, A., 2013. Serpentinite: What, why, where? *Elements* 9, 99–
530 106. doi:10.2113/gselements.9.2.99

531 Farmer, V.C., 1974. *Infrared Spectra of Minerals*. Mineral. Soc. London 149–151.
532 doi:10.1180/mono-4

533 Felmy, A.R., Cho, H., Rustad, J.R., Mason, M.J., 2001. An aqueous thermodynamic model for
534 polymerized silica species to high ionic strength. *J. Solution Chem.* 30, 509–525.
535 doi:10.1023/A:1010382701742

536 Frost, R.B., Beard, J.S., 2007. On silica activity and serpentinization. *J. Petrol.* 48, 1351–1368.
537 doi:10.1093/petrology/egm021

538 Früh-Green, G.L., Orcutt, B.N., Green, S., Cotterill, C., 2016. Expedition 357 Preliminary
539 Report Atlantis Massif Serpentinization and Life.

540 Gunnarsson, I., Arnórsson, S., 2000. Amorphous silica solubility and the thermodynamic
541 properties of $\text{H}_4\text{SiO}_4^\circ$ in the range of 0° to 350°C at P(sat). *Geochim. Cosmochim. Acta* 64,
542 2295–2307. doi:10.1016/S0016-7037(99)00426-3

543 Harrison, A.L., Power, I.M., Dipple, G.M., 2013. Accelerated carbonation of brucite in mine
544 tailings for carbon sequestration. *Environ. Sci. Technol.* 47, 126–134.
545 doi:10.1021/es3012854

546 Helgeson, H.C., Murphy, W.M., Aagaard, P., 1984. Thermodynamic and kinetic constraints on
547 reaction rates among minerals and aqueous solutions. II. Rate constants, effective surface

548 area, and the hydrolysis of feldspar. *Geochim. Cosmochim. Acta* 48, 2405–2432.
549 doi:10.1016/0016-7037(84)90294-1

550 Kadko, D., Butterfield, D.A., 1998. The relationship of hydrothermal fluid composition and
551 crustal residence time to maturity of vent fields on the Juan de Fuca Ridge. *Geochim.*
552 *Cosmochim. Acta* 62, 1521–1533. doi:10.1016/S0016-7037(98)00088-X

553 Katayama, I., Kurosaki, I., Hirauchi, K. ichi, 2010. Low silica activity for hydrogen generation
554 during serpentinization: An example of natural serpentinites in the Mineoka ophiolite
555 complex, central Japan. *Earth Planet. Sci. Lett.* 298, 199–204.
556 doi:10.1016/j.epsl.2010.07.045

557 Kelley, D.S., 2005. A Serpentinite-Hosted Ecosystem: The Lost City Hydrothermal Field.
558 *Science* (80-.). 307, 1428–1434. doi:10.1126/science.1102556

559 Klein, F., Bach, W., Jöns, N., McCollom, T., Moskowicz, B., Berquó, T., 2009. Iron partitioning
560 and hydrogen generation during serpentinization of abyssal peridotites from 15°N on the
561 Mid-Atlantic Ridge. *Geochim. Cosmochim. Acta* 73, 6868–6893.
562 doi:10.1016/j.gca.2009.08.021

563 Kong, X.Z., Tutolo, B.M., Saar, M.O., 2013. DBCreate: A SUPCRT92-based program for
564 producing EQ3/6, TOUGHREACT, and GWB thermodynamic databases at user-defined T
565 and P. *Comput. Geosci.* 51, 415–417. doi:10.1016/j.cageo.2012.08.004

566 Kump, L.R., Barley, M.E., 2007. Increased subaerial volcanism and the rise of atmospheric
567 oxygen 2.5 billion years ago. *Nature* 448, 1033–6. doi:10.1038/nature06058

568 Lichtner, P.C., Hammond, G.E., Lu, C., Karra, S., Bisht, G., Andre, B., Mills, R.T., Kumar, J.,
569 Frederick, J.M., 2017. PFLOTRAN Web page.

570 Lin, F.C., Clemency, C. V., 1981. The dissolution kinetics of brucite, antigorite, talc, and
571 phlogopite at room temperature and pressure. *Am. Mineral.* 66, 801–806.

572 Ludwig, K.A., Kelley, D.S., Butterfield, D.A., Nelson, B.K., Früh-Green, G., 2006. Formation
573 and evolution of carbonate chimneys at the Lost City Hydrothermal Field. *Geochim.*
574 *Cosmochim. Acta* 70, 3625–3645. doi:10.1016/j.gca.2006.04.016

575 Luhmann, A.J., Kong, X.Z., Tutolo, B.M., Garapati, N., Bagley, B.C., Saar, M.O., Seyfried,
576 W.E., 2014. Experimental dissolution of dolomite by CO₂-charged brine at 100°C and 150
577 bar: Evolution of porosity, permeability, and reactive surface area. *Chem. Geol.* 380, 145–
578 160. doi:10.1016/j.chemgeo.2014.05.001

579 Luhmann, A.J., Tutolo, B.M., Bagley, B.C., Mildner, D.F.R., Scheuermann, P., Feinberg, J.,
580 Seyfried, W.E., 2017. Chemical and physical changes during seawater flow through intact
581 dunite cores: An experimental study at 150–200°C. *Geochim. Cosmochim. Acta.*
582 doi:10.1016/j.gca.2017.07.020

583 Maher, K., Steefel, C.I., DePaolo, D.J., Viani, B.E., 2006. The mineral dissolution rate
584 conundrum: Insights from reactive transport modeling of U isotopes and pore fluid
585 chemistry in marine sediments. *Geochim. Cosmochim. Acta* 70, 337–363.
586 doi:10.1016/j.gca.2005.09.001

587 Martin, B., Fyfe, W.S., 1970. Some experimental and theoretical observations on the kinetics of
588 hydration reactions with particular reference to serpentinization. *Chem. Geol.* 6, 185–202.
589 doi:10.1016/0009-2541(70)90018-5

590 Martin, W., Baross, J., Kelley, D., Russell, M., 2008. Hydrothermal vents and the origin of life.
591 *Nat. Rev. Microbiol.* 6, 805–814. doi:10.1038/nrmicro1991

592 Mullin, J.B., Riley, J.P., 1955. The colorimetric determination of silicate with special references
593 to sea and natural water. *Anal. chim. Acta* 12, 162–176.

594 Noiriél, C., Luquot, L., Madé, B., Raimbault, L., Gouze, P., Van Der Lee, J., 2009. Changes in
595 reactive surface area during limestone dissolution: An experimental and modelling study.
596 *Chem. Geol.* 265, 160–170.

597 O’Hanley, D.S., 1996. *Serpentinites*. Oxford University Press.

598 Oze, C., Sharma, M., 2005. Have olivine, will gas: Serpentinization and the abiogenic production
599 of methane on Mars. *Geophys. Res. Lett.* 32, 1–4. doi:10.1029/2005GL022691

600 Palandri, J.L., Kharaka, Y.K., 2004. A compilation of rate parameters of water-mineral
601 interaction kinetics for application to geochemical modeling. *USGS Open File Rep.* 2004–
602 1068, 71. doi:10.1098/rspb.2004.2754

603 Pokrovsky, O.S., Schott, J., 2004. Experimental study of brucite dissolution and precipitation in
604 aqueous solutions: Surface speciation and chemical affinity control. *Geochim. Cosmochim.*
605 *Acta* 68, 31–45. doi:10.1016/S0016-7037(03)00238-2

606 Rimstidt, J.D., 2014. *Geochemical Rate Models*. Cambridge University Press, Cambridge, UK.

607 Rimstidt, J.D., 1997. Quartz solubility at low temperatures. *Geochim. Cosmochim. Acta* 61,
608 2553–2558. doi:10.1016/S0016-7037(97)00103-8

609 Rimstidt, J.D., Barnes, H.L., 1980. The kinetics of silica-water reactions. *Geochim. Cosmochim.*
610 *Acta*. doi:10.1016/0016-7037(80)90220-3

611 Rimstidt, J.D., Brantley, S.L., Olsen, A.A., 2012. Systematic review of forsterite dissolution rate
612 data. *Geochim. Cosmochim. Acta* 99, 159–178. doi:10.1016/j.gca.2012.09.019

613 Robie, R.A., Hemingway, B.S., 1995. Thermodynamic properties of minerals and related
614 substances at 298.15 K and 1 bar (105 Pascals) pressure and at higher temperatures.

615 Rüpke, L.H., Morgan, J.P., Hort, M., Connolly, J.A.D., 2004. Serpentine and the subduction
616 zone water cycle. *Earth Planet. Sci. Lett.* 223, 17–34. doi:10.1016/j.epsl.2004.04.018

617 Russell, J.D., Fraser, A.R., 1994. Infrared methods. *Clay Mineral. Spectrosc. Chem. Determ.*
618 *Methods* 11–67. doi:10.1007/978-94-011-0727-3_2

619 Saldi, G.D., Köhler, S.J., Marty, N., Oelkers, E.H., 2007. Dissolution rates of talc as a function
620 of solution composition, pH and temperature. *Geochim. Cosmochim. Acta* 71, 3446–3457.
621 doi:10.1016/j.gca.2007.04.015

622 Schrenk, M.O., Brazelton, W.J., Carolina, N., Lang, S.Q., 2013. Serpentinization, Carbon, and
623 Deep Life. *Rev. Mineral.* 75, 575–606. doi:10.2138/rmg.2013.75.18

624 Seyfried, W.E., Pester, N.J., Tutolo, B.M., Ding, K., 2015. The Lost City hydrothermal system:
625 Constraints imposed by vent fluid chemistry and reaction path models on subseafloor heat
626 and mass transfer processes. *Geochim. Cosmochim. Acta* 163, 59–79.
627 doi:10.1016/j.gca.2015.04.040

628 Sleep, N.H., Bird, D.K., Pope, E.C., 2011. Serpentinite and the dawn of life. *Philos. Trans. R.*
629 *Soc. B* 366, 2857–2869. doi:10.1098/rstb.2011.0129

630 Sojo, V., Herschy, B., Whicher, A., Camprubi, E., Lane, N., 2016. The origin of life in alkaline
631 hydrothermal vents. *Astrobiology* 16, 181–197. doi:10.1089/ast.2015.1406

632 Sverjensky, D.A., Harrison, B., Azzolini, D., 2014. Water in the deep Earth: The dielectric
633 constant and the solubilities of quartz and corundum to 60kb and 1200°C. *Geochim.*

634 Cosmochim. Acta 129, 125–145. doi:10.1016/j.gca.2013.12.019

635 Syverson, D.D., Tutolo, B.M., Borrok, D.M., Seyfried, W.E., 2017. Serpentinization of olivine at
636 300 °C and 500 bars: An experimental study examining the role of silica on the reaction
637 path and oxidation state of iron. Chem. Geol. 475, 122–134.
638 doi:10.1016/j.chemgeo.2017.11.006

639 Tutolo, B.M., Luhmann, A.J., Kong, X.Z., Saar, M.O., Seyfried, W.E., 2015. CO₂ sequestration
640 in feldspar-rich sandstone: Coupled evolution of fluid chemistry, mineral reaction rates, and
641 hydrogeochemical properties. Geochim. Cosmochim. Acta 160, 132–154.
642 doi:10.1016/j.gca.2015.04.002

643 Tutolo, B.M., Mildner, D.F.R., Gagnon, C.V.L., Saar, M.O., Seyfried, W.E., 2016. Nanoscale
644 constraints on porosity generation and fluid flow during serpentinization. Geology 44, 103–
645 106. doi:10.1130/G37349.1

646 Tutolo, B.M., Tosca, N.J., in review Experimental examination of Mg-silicate - carbonate
647 interactions during lacustrine carbonate reservoir formation.

648 Waite, J.H., Glein, C.R., Perryman, R.S., Teolis, B.D., Magee, B.A., Miller, G., Grimes, J.,
649 Perry, M.E., Miller, K.E., Bouquet, A., Lunine, J.I., Brockwell, T., Bolton, S.J., 2017.
650 Cassini finds molecular hydrogen in the Enceladus plume: Evidence for hydrothermal
651 processes. Science (80-.). 356, 155–159. doi:10.1126/science.aai8703

652 White, A.F., Peterson, M.L., 1990. Role of reactive-surface-area characterization in geochemical
653 kinetic models. Chem. Model. Aqueous Syst. II (eds DC Melchoir RL Bassett) Chap 35,
654 461–475.

655 York, D., Evensen, N.M., Martínez, M.L., De Basabe Delgado, J., 2004. Unified equations for

656 the slope, intercept, and standard errors of the best straight line. *Am. J. Phys.* 72, 367.

657 doi:10.1119/1.1632486

658 Zarubin, D.P., Nemkina, N.V., 1990. The solubility of amorphous silica in an alkaline aqueous

659 medium at a constant ionic strength. *Russ. J. Inorg. Chem.*

660